ADVANCED FUNCTIONAL MATERIALS
www.afm-journal.de

Carbon Materials With Conductivity Gradients Allow Dynamic Screening of Steep Temperature Differences Along Thin Films

*Alexander Berger, Marius Schöttle, Flora Lebeda, Holger Schmalz, Peter Bösecke, Sabine Rosenfeldt, Andreas Greiner, and Markus Retsch**

Carbon materials comprise a wide range of microstructures and excellent electrical and thermal properties while being cost-effective and readily available. They can be obtained through carbothermal processes at high temperatures, starting from cellulose. Catalytically active compounds, for example, iron salts, strongly influence the carbon microstructure during the graphitization process. Different degrees of structural order can, therefore, be achieved by adjusting the concentration of the iron salts. An infusion withdrawal impregnation approach is used on filter paper to prepare a continuous gradient of the carbon microstructure. This structural change is accompanied by a continuous variation of the closely related electrical and thermal transport properties. Even more, the synergistic interplay of local sheet resistance and thermal diffusivity results in the formation of switchable temperature gradients when an external current is applied. Steady state temperature differences of up to 80 °C are observed along the centimeter-scaled samples. The controllable temperature gradient formation will be of great interest for applications requiring a fast temperature screening. Furthermore, the temperature gradient can be imposed onto other materials, which will be particularly relevant for advanced thin film characterization applications.

1. Introduction

Functional gradient materials (FGM) are characterized by a continuous variation of one or more physicochemical properties along a certain spatial direction. The local variation of a material's nano- or mesostructure, composition, or surface properties can translate into interesting mechanical, optical, thermal, catalytic, electric, acoustic, or wetting properties. FGMs can be found in nature and have increasingly gained the interest of materials scientists.[1] For example, mechanically graded materials have been demonstrated to improve the cycling stability of lithium metal batteries[2] or render ultrahigh-molecular weight polyethylene impact-resistant.[3] Graphite materials are a particularly interesting and versatile class of materials. Inspiring examples of the fascinating possibilities provided by gradually structured materials have been reported for functionally graded carbon materials (FGCM). Hard carbon nanoparticles

A. Berger, M. Schöttle, F. Lebeda, S. Rosenfeldt, M. Retsch
Department of Chemistry
Physical Chemistry I
University of Bayreuth
Universitätsstr. 30, 95447 Bayreuth, Germany
E-mail: markus.retsch@uni-bayreuth.de
H. Schmalz, A. Greiner
Department of Chemistry
Macromolecular Chemistry II
University of Bayreuth
Universitätsstr. 30, 95447 Bayreuth, Germany
The ORCID identification number(s) for the author(s) of this article can be found under https://doi.org/10.1002/adfm.202400740

DOI: 10.1002/adfm.202400740

P. Bösecke
European Synchrotron Radiation Facility (ESRF)
71 Avenue des Martyrs, CS 40220, 38043 Grenoble Cedex 9, France
A. Greiner
Keylab for Synthesis and Molecular Characterization
Bavarian Polymer Institute (BPI)
Universitätsstraße 30, 95447 Bayreuth, Germany
M. Retsch
Bavarian Center for Battery Technology (BayBatt)
Weiherstraße 26, 95448 Bayreuth, Germany
M. Retsch
Bavarian Polymer Institute (BPI)
Bayreuth Center for Colloids and Interfaces (BZKG)
Universitätsstraße 30, 95447 Bayreuth, Germany

with a gradient microstructure have been used as micro-supercapacitors.[4] The introduction of porosity gradients by ultracentrifugation and colloidal templating has led to several interesting studies. LiO_2 In addition to improved capacity, batteries based on porous FGCM also show orientation dependence of the capacitance.[5] This method can also be extended by incorporating magnetic nanoparticles, leading to anisotropic magnetization.[6] The addition of graded chemical functionality[7] opened an even wider parameter space, leading to the prospects of molecule-specific transport.[8] The preparation of such FGCM requires sophisticated methods and strongly depends on the carbon source.

In this context, cellulose represents an interesting carbon source, since it is the most abundant naturally produced material on the planet.[9] Materials made from cellulose, like textiles or paper, have been used by humanity for thousands of years.[10] The carbohydrate can exceed a chain length from 300 to 10 000 repeating units depending on the origin. Due to hydrogen bonding, its typical hierarchical, supramolecular structure is formed, from which several fields of application and functions have been derived.[11,12] Paper is the most prominent material made from cellulose. It is widely used in everyday life and is fully recyclable.[13] Besides its typical utilization for packaging or printing, new applications such as printed electronics or flexible substrates for light-emitting devices have attracted strong interest over the last few years.[14–17] Quite recently, paper has been equipped with a polymer gradient across the entire thickness, resulting in moisture-sensitive actuating sheets.[18]

Cellulose materials, particularly paper, also qualify as a source of carbon materials (CM).[19,20] CMs feature a variety of superiorities such as a range of different microstructures,[21] electrical,[22–24] and thermal properties,[25] good chemical stability,[21] non-toxicity,[26] and low-cost.[27] Promising fields for CMs are organic or photocatalysis.[28,29] Due to their electrical properties, they also are prominent in the field of energy storage devices.[30,31] Solar thermal energy conversion takes advantage of CM's excellent thermal properties and unique meso- and nanostructure,[32,33] which is especially of interest for desalination of seawater[34] or heat dissipation.[25]

CMs are accessible with natural materials through carbonization processes.[35] For example, hydrothermal carbonization is conducted in a pressurized vessel at relatively low temperatures.[36] During this process, the original mesostructure is not retained.[37] With the process of classic high-temperature carbonization at 2500 °C, preservation of the original structure is more likely due to the absence of water during heating.[38] Catalytic carbonization was developed to avoid high temperatures and reduce cost and energy.[39] By the presence of active catalytic compounds like transition metals such as Fe, Co, Ni, or Mn,[40,41] the temperature can be reduced by at least 1000 K.[42] Other groups have already shown, that the application of Fe results in the highest catalytic efficiency.[43,44]

Through catalytic carbonization of wood-derived feedstock, applications like supercapacitors are feasible.[45] Cavities occur during the process due to iron residues, which increase the surface area and enhance the specific capacitance while showing excellent cycling stability. Furthermore, other material classes such as carbon spheres,[46] sponges,[47] fibrils,[48] aerogels,[49] or quantum dots[50] can be derived from the catalytic carbonization of wood or wood related compounds. In many cases, the catalyst is impregnated into the carbonaceous precursor via an aqueous solution of the respective salt. This opens the possibility of creating fine structures by controlling the precursor impregnation, e.g., by an inkjet printer. In the case of an iron catalyst and filter paper, this has been shown to create carbon-based electrodes.[51]

Instead of controlling the local concentration of $FeCl_3$ as shown by Glatzel et al.[51], we outline the marked influence of the $FeCl_3$ concentration on the structural order of the resulting CM. This provides unique access to an FGCM with gradual changes in thermal and electric conductivity. By utilizing infusion withdrawal coating[52] we achieve a structural gradient on the centimeter scale. This way, plain filter paper can be converted into a FGCM with distinct thermal and electrical properties. Most intriguingly, applying an electric current allows the generation of controllable and switchable temperature gradients. This way, we achieve a temperature difference across the CM of up to $\Delta T = 80\,°C$ within seconds. Such temperature gradient heaters are of particular interest for temperature-dependent structure parameters and their kinetic evolution,[53,54] battery research,[55,56] microfluidics[57,58] and continuous flow polymerase chain reaction.[59,60]

2. Results and Discussion

Catalytic carbonization is a well-known method for enhancing crystallinity during the graphitization of carbon-rich precursors. Homogeneously impregnated filter papers are prepared as references. Our method (Figure S1, Supporting Information) uses standard laboratory-grade filter paper as a carbon precursor. It is submerged in ferric chloride ($FeCl_3$) (0.1 to 3 M) solution, which acts as a catalytic active compound. The impregnated samples are dried and carbonized under an inert atmosphere at 1500 °C. Scanning electron microscopy (SEM) measurements performed directly after carbonization (**Figure 1a**) show the formation of iron nanoparticles with a size range of roughly 100 to 600 nm on the fiber surface and inside of them. Catalyst-treated samples are subsequently washed with concentrated hydrochloric acid to remove residual iron nanoparticles from the carbon structure after the heating step (Figure 1b). The fiber structure of the paper is preserved during carbonization. However, we observe differences between the carbonized filter paper without a catalyst and the one impregnated with ferric chloride. Laser scanning confocal microscopy in Figure S2 (Supporting Information) reveals a significant shrinkage of the fiber structure of the untreated filter paper. The impregnated paper remains nearly unchanged after carbonization. Thus, the preservation of the original structure makes it easier to design new mesostructures in CMs. SEM images (Figure 1a) show that the iron residue covers a large portion of the fibers and even infiltrates them. This is consistent with the proposed mechanism of catalytic graphitization, which has been investigated by various characterization methods, including (in situ) transmission electron microscopy.[39,45,51] Gomez-Martin et al. published an extensive study in which they stated that iron is formed due to the thermal decomposition of $FeCl_3$ with various intermediate oxides. Under the presence of the metallic Fe Fe_3C forms, resulting in the graphitization process. At higher temperatures than 750 °C, the carbide phase decomposes to metallic Fe again. At even higher temperatures >800 °C, another mechanism

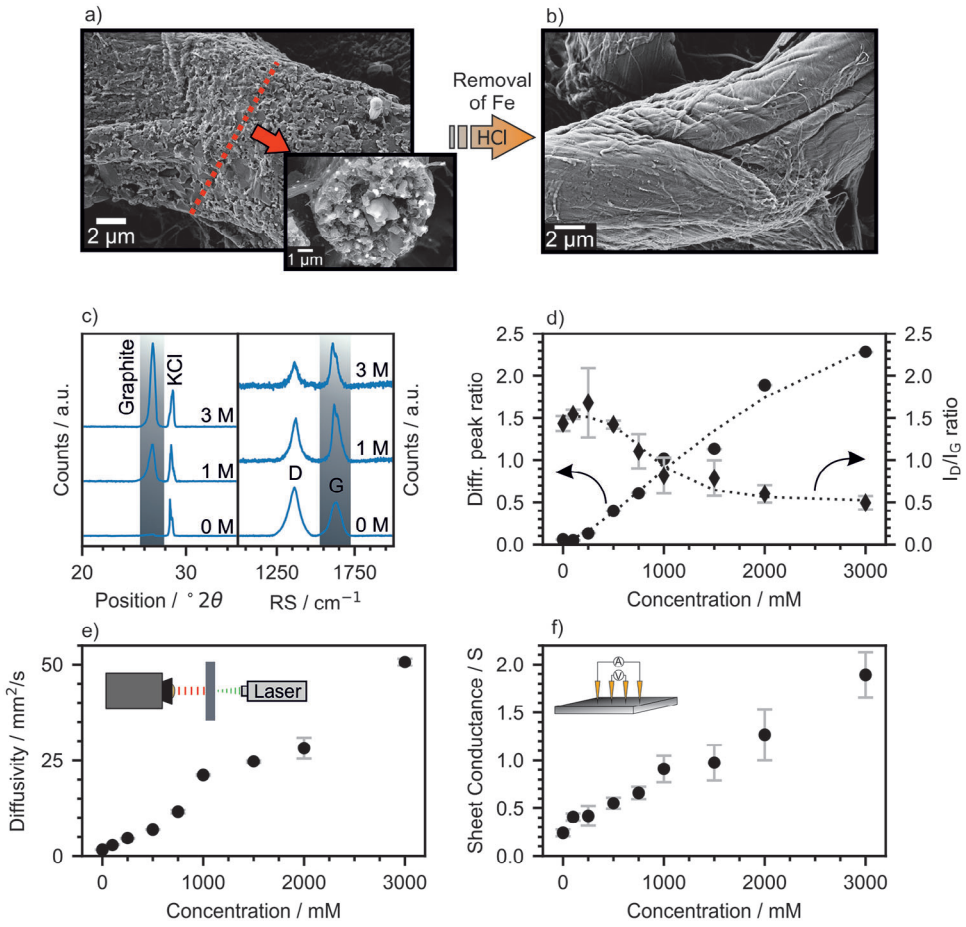

Figure 1. Investigation of the influence of ferric chloride on filter paper carbonization. a) Detailed SEM image of a carbonized fiber from an impregnated filter paper (1 M). The inset shows a fiber cross-section with chemical contrast from backscattering electrons. b) SEM image of a fiber after acid treatment. The surface is smoother compared to (a), indicating iron removal. c) XRD and Raman measurements of the concentration variation as reference. All curves are baseline-corrected. The XRD data is normalized to KCl (200) reflection peak. The Raman data shows disordered (D) and graphitic (G) bands, resembling amorphous and crystalline carbon. The diffraction peak ratio and the intensity ratio of D and G band are plotted in (d). With rising iron content, the graphitic reflection peak increases while the D/G intensity ratio decreases. Both indicate the growth of crystalline structures. e) Lock-in thermography of the concentration sweep shows a large diffusivity range from nearly zero up to 50 $mm^2\ s^{-1}$ with a continuous increase. f) The electrical conductance shows a similar trend with an increase by a factor of ten.

involving the precipitation of 3D graphite crystals by the catalyst particle takes place.[39]

We assume that the ferric chloride and its products stabilize the mesostructure during heating, preventing carbonization-induced shrinkage and keeping it in its original shape. As we want to examine the properties of a purely carbonaceous material rather than a composite, the residual iron in the structure is removed via etching with hydrochloric acid. The resulting fiber, shown in Figure 1b, strongly resembles the original cellulose fibers from Figure S3a,b (Supporting Information). Comparing the fiber thickness, we can carve out the differences between the use of catalyst and reference. The thickness histogram visualizes the previously mentioned shrinkage of the non-impregnated fibers during carbonization. While the thickness of the pristine filter paper (Figure S3c, Supporting Information) is reduced by 47% in mean from 16.5 ± 5.2 µm to 8.7 ± 2.5 µm, the mean reduction of the impregnated samples (Figure S3d) is only by 11% (23.0 ± 8.0 µm to 20.4 ± 8.0 µm). Thermogravimetric measurements (Figure S3e) confirm significant differences in the carbonization behavior. Pristine filter paper shows a single step in the heating process, which can be referred to as the decomposition of cellulose.[39] However, the carbonization of the impregnated samples consists of two steps. The first until 460 °C is also referred to as the decomposition of cellulose. The second significant drop in mass at 600 °C is caused by the carbothermal reduction to elemental iron and the formation of graphitic carbon.[51] Differences in residual mass, 13.8% for 0 M and 31.7% for 1 M, arise from the iron residues in the impregnated samples and the different carbonization processes. Those divergent carbonization mechanisms are probably the reason for the fiber shrinkage discussed earlier.

The relevance of the catalytic contribution of the $FeCl_3$ is emphasized by X-ray diffraction (XRD) and wide-angle X-ray (WAXS) (Figure S4). The filter paper exhibits a typical cellulose pattern. The large reflection peak at $2\theta = 22.7°$ is attributed to cellulose (200).[61] The carbonization without $FeCl_3$ leads to

mainly amorphous carbon with broad reflection peaks. The presence of $FeCl_3$ results in a large carbon (002) reflection peak at $2\theta = 26°$, as well as a prominent α-Fe (110) peak at $2\theta = 44.5°$ with several smaller peaks, referred to as carbon, or carbide structures.[61–63] The presence of iron encourages the proposed mechanism discussed earlier. The irons' concomitant X-ray fluorescence causes the observed background radiation that can be removed via acid treatment.

We performed a concentration sweep of the $FeCl_3$ impregnation (Figure S5a, Supporting Information) as a reference for the gradient CM that will be discussed later. SEM images of (fiber) cross-sections (Figure S5b–g, Supporting Information) of carbonized 0, 1 and 3 M samples after iron removal show significant differences between the fiber morphology. The fiber interior exhibits an increasing degree of granularity, with the not-impregnated sample having the most homogeneous appearance and the highest $FeCl_3$ being the most heterostructured fiber. Concomitantly, the presence of fibrillar structures on the cellulose fiber surface vanishes and is replaced by smeared-out droplets. We refer the changes of the fiber surface to partial cellulose hydrolysis at the acidic pH of the $FeCl_3$ solution. Further, the grainy interior of the fibers hints toward an increased structural order and crystallite size. Raman and XRD highlight the change in crystallinity (Figure 1c; Figure S6, Supporting Information). For XRD, we added KCl as an internal reference substance to quantify the graphite reflection peak. By normalizing the data on the KCl (200) peak, we observe a significant increase in the carbon crystallinity. A similar trend occurs in Raman spectroscopy. Here, we compare the intensity of disordered D- and graphitic G-band. Since the latter arises from longitudinal vibrations between graphite layers, it can be seen as a measure of structural order in CMs. The ratios of XRD peaks and Raman band intensities (Figure 1d) show both a significant change with an increasing amount of iron catalyst in the system. While the diffraction peak ratio increases to a value of two, the Raman intensity ratio is decreased by two-thirds. Further, a ratio below one indicates more graphitic than amorphous content. With the Tuinstra and König relation, we calculated the crystallite size L_a.[64] It uses the I_D/I_G ratio, that is inverse proportional to L_a. For the ratios at 0, 1 and 3 M, we get a crystallite size of 27.2, 47.8 and 79.0 nm, respectively. According to the literature, these are similar size ranges to heat-treated nano-graphite[65] or synthetic graphite.[20]

We observe a similar trend in WAXS experiments (Figure S7, Supporting Information). To get an idea of the mesoscopic structure of the impregnated filter papers, they are further characterized with small angle X-ray scattering (SAXS). The slope from the scattering data (Figure S7a, Supporting Information) at low q values (<0.3 nm) is increasing with the ferric concentration. The absence of iron leads to $q^{-1.9}$, whereas high concentrations (>1M) have steeper slopes of $q^{-3.4}$ (Figure S7b, Supporting Information), indicating different porosity. We infer that the cross-over points between low q and intermediate q scaling indicate hierarchical levels (correlation sizes) in the fibers. For the absence of iron, those structures are in the size of 22.4 nm (ii). For 0.253 M, they are about 36.7 and 41.9 nm (i), which indicates a change in microstructure due to the addition of $FeCl_3$. Overall, the structural analysis of the non-impregnated samples as a reference shows that the presence of $FeCl_3$ is pivotal in generating crystalline domains. The correlation sizes increase with the catalyst concentration and seem to be accompanied by an increase in porosity.

We now investigate the thermal and electric conductivity of the reference samples. With lock-in thermography (LIT), we obtain the in-plane thermal diffusivity as a measure of the heat transfer rate in a material.[66] It is derived using the slope method of a line laser setup with the amplitude A and the phase ϕ.[67] The values for the thermal diffusivity α for the different catalyst concentrations are shown in Figure 1e. They feature a constant change in concentration. The diffusivity at 0 M amounts to 1.6 $mm^2\ s^{-1}$. It increases linearly up to 47.7 $mm^2\ s^{-1}$ at 3 M, which is a factor 30 higher than without catalyst. For a better comparison, we measured the specific heat capacity c_p and density ρ of 0, 1 and 3 M samples. The c_p did not change significantly with $FeCl_3$. The average c_p is 0.82 ± 0.08J $g^{-1}\ K^{-1}$. The density, measured by a helium pycnometer, is 1.53 ± 0.03 g cm^{-3}, 1.71 ± 0.03 g cm^{-3} and 1.9 ± 0.04 g cm^{-3} for the three concentrations, respectively. With the expression $\kappa = \alpha \rho c_p$, the thermal conductivity κ results in 2.0 ± 0.2 W $m^{-1}\ K^{-1}$, 30 ± 3 W $m^{-1}\ K^{-1}$ and 79 ± 8 W $m^{-1}\ K^{-1}$. Setting this in context, highly crystalline pyrolytic graphite exceeds 1000 $mm^2\ s^{-1}$ (1500 W $m^{-1}\ K^{-1}$) parallel to its layers or around 6 $mm^2\ s^{-1}$ (9 W $m^{-1}\ K^{-1}$) perpendicular to them.[68] Comparable thermally treated materials are in the same range as ours from 0.8 to 50 $mm^2\ s^{-1}$.[69–71] PAN-based carbon fibers have been reported with a range of thermal conductivity from 5 to ≈65 W $m^{-1}\ K^{-1}$, depending on their tensile modulus.[72] Pitch-based carbon fibers reach up to ≈1000 W $m^{-1}\ K^{-1}$.[73]

Since the impregnated papers are fairly thin, it is reasonable to measure their electrical properties with a four-point probe setup (Figure 1f). We were able to produce non-impregnated samples with a sheet conductance of 0.26 S. At the highest concentration of $FeCl_3$, we observe values of 2 S. Consequently, the treatment with ferric chloride increases the sheet conductance by a factor of ≈7.7, which is significantly lower compared to the increase in thermal diffusivity. However, the increase with rising catalyst content is consistent with the literature.[62] Han et al. produced flexible graphite/graphene films on which they measured a similar electrical conductivity.[74] Commercial graphite sheets feature conductivities of 1.1×10^3 to 4.5×10^3 S cm^{-1},[75] that is around a magnitude higher than the 3 M sample with 2×10^2 S cm^{-1} and an estimated thickness of 100µm. To summarize, the structural changes caused by adding ferric chloride contribute differently to the variation of the thermal and electric transport properties. The increase in crystallinity and crystallite size apparently enhances the thermal conduction more strongly than the electric one. A similar influence of the grain size on the conduction properties has been reported in the literature.[76,77] Ma et al. provided an interpretation of this observation based on different transmission rates of phonons and electrons at the grain boundaries for the case of graphene. There, the thermal conductivity increased by a factor of ≈8.5, while the electric conductivity only increased by a factor of ≈2.4.[78] The presence of amorphous carbon in the case of reduced graphene oxide introduces further complexity to the interplay between grain size and transport properties.[79] Owing to the catalytic treatment and low amount of amorphous structures of the samples presented here, we rationalize the differences in heat and electron transport in accordance with Ma et al.[78] as an effect of the transmission rate differences at the grain boundaries.

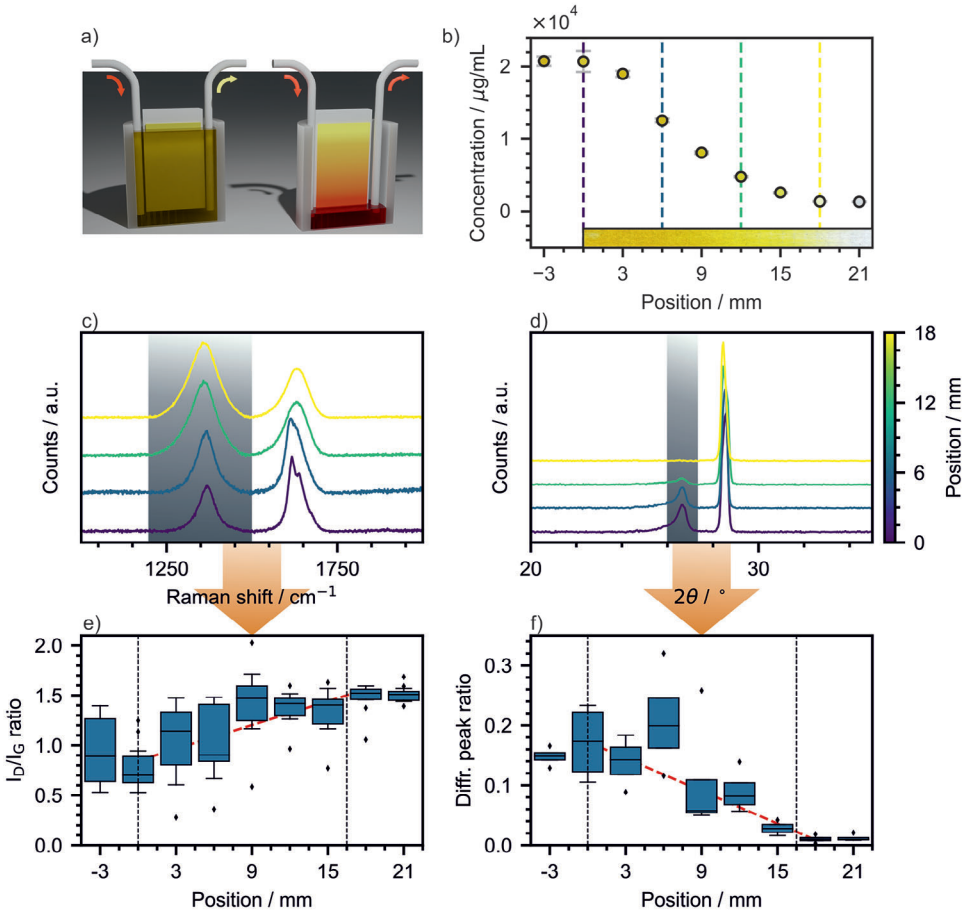

Figure 2. Structural characterization of the gradient-impregnated filter paper. a) Illustration of the gradient preparation with the infusion withdrawal setup. b) Iron species distribution along the gradient. Concentrations were measured with AAS. The dotted lines show the positions of the depicted XRD and Raman measurements. XRD patterns c) and Raman spectroscopy d) of different positions on the sample. e) The intensity ratios I_D/I_G were derived from c). The red dashed line acts as a guide to the eye for the gradient regime. f) The carbon (002) reflection peak is analyzed relative to the KCl (200) peak shown in d). A gradual change can be observed.

Capitalizing on the direct relation between the $FeCl_3$ concentration, the graphitic microstructure, and its related transport properties, we can now fabricate a graphitic film with a controllable structure and property gradient. We control the formation using "infusion withdrawal coating", which was recently published by Schöttle et al. for gradient colloidal crystals and glasses.[52,80,81] Core of that method are two separate syringe pumps (**Figure** 2a), ensuring finely adjusted pumping rates. A filter paper is mounted inside a container filled with water. One pump fills the ferric chloride solution at a constant rate. The other withdraws it at a higher rate. The difference in the pumping rates causes the $FeCl_3$ concentration to rise while simultaneously lowering the level of the liquid (Figure S8a, Supporting Information). Hence, the amount of $FeCl_3$ impregnated into the filter paper changes along the coating direction. We measured the iron distribution of a gradient sample with atomic absorption spectroscopy (AAS) (Figure 2b). The initial water level is set to 16 mm, which represents the lowest $FeCl_3$ concentration and marks one boundary. The other boundary (0 mm) corresponds to the point where the process is terminated, with the highest $FeCl_3$ concentration (≈1 M $FeCl_3$). We find that, similar to the reference samples, the gradient can be observed by the intensity of its yellow color. However, due to diffusion effects at the top, the yellow color spreads in the white area, which was not in contact with the ferric chloride solution. Further, we did not observe any additional gradients perpendicular to the dipping direction (see Section S1 and Figure S9, Supporting Information). Across the paper thickness (z-axis, 100 to 200 µm), the ferric chloride can entirely diffuse through the material within the given impregnation time. Along the paper plane (y-axis), the presence of the water meniscus ensures that the whole width of the paper is homogeneously impregnated with the ferric chloride solution.

Raman and XRD were measured to confirm the successful gradient formation. We observe a gradual, linear increase of the G-band for increasing $FeCl_3$ concentration, which corresponds to positions left of the 16 mm boundary (Figure 2c, e). The ratio decreases by a factor of two. Compared to the reference samples, this range of the intensity ratio corresponds to a concentration of 0.1 to 1 M. In addition to the measurements along the gradient, we also performed Raman measurements perpendicular to it (Figure S9, Supporting Information). Along the

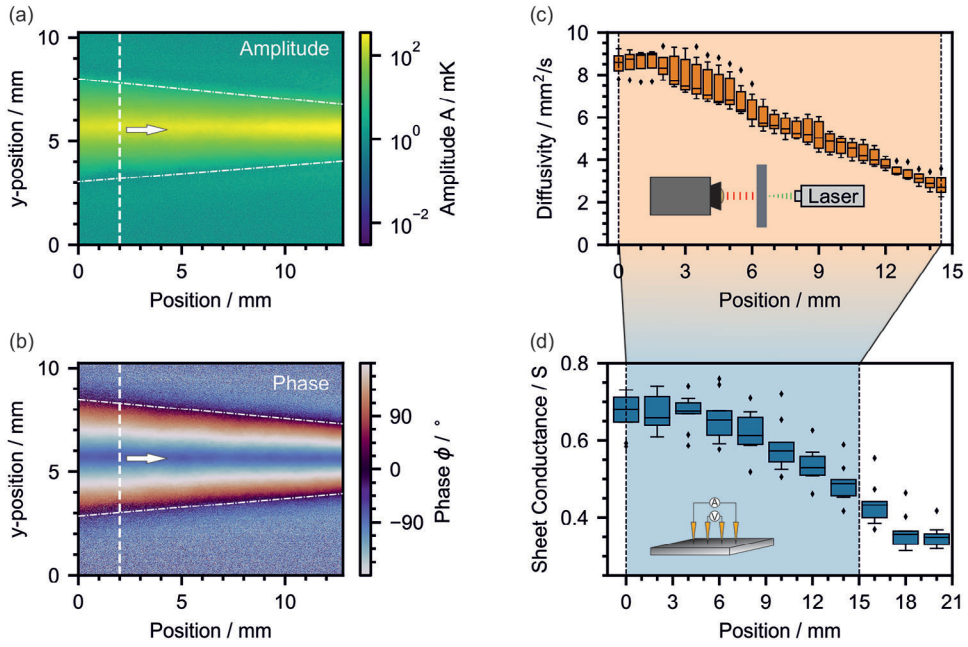

Figure 3. Position-dependent conduction properties of the gradient samples. Amplitude a) and phase b) of lock-in thermography measurements. The dotted lines and the arrows visualize the direction of the position-dependent evaluation. The fitted data are summarized in (c). The thermal diffusivity shows a monotonic decreasing trend along the gradient. d) Sheet conductance from four-point probe electrical measurements decreases systematically along the carbon gradient.

y- and z-direction, we found no systematic variation of the I_D/I_G ratio.(Figures S10 and S11, Supporting Information) As observed for the gradient along the dip-coating direction, the spread of the I_D/I_G ratio increases with a higher degree of graphitization. In XRD measurements, KCl serves as a reference for normalization. The graphite (002) reflection peak at 26° increases its intensity (Figure 2d) accordingly to the increase in $FeCl_3$ concentration. We observe a linear growth from nearly 0 to 0.2. Since the carbon (002) peak is still slightly present for non-catalytic carbonization (Figure S4a, Supporting Information), it does not start from zero intensity. Furthermore, the position of the (002) peak remains unchanged with increasing $FeCl_3$ content (Figure S12, Supporting Information), resulting in a consistent basal plane spacing of approximately 3.3Å for the graphite sheets, which aligns with the findings of Maldonado-Hódar et al.[43] In WAXS measurements (Figure S13, Supporting Information), we see a comparable linear trend for the (002) peak intensity. Regarding SAXS data from the same measurements, there is a change in the slope at a small q regime. For low q, we observe a linear change from q^{-3} to $q^{-2.2}$, that indicates a reduction in materials porosity. Further, the data show a cross-point (i) on position 16 mm at $q = 0.42$ nm^{-1}, that corresponds to 15 nm in real space. The cross-over point then shifts continuously toward lower q with increasing $FeCl_3$ concentration. All in all, the measurements underline the gradual change in the carbon structure. The graphitization process introduces considerable brittleness to the graphitic thin film. We did not observe a macroscopic influence of the microstructural gradient on the mechanical properties. Owing to the interwovenness of the fibrous graphite structure, the gradient samples can be bent without irreversible cracking (Figure S8b, Supporting Information).

LIT is utilized to resolve the thermal diffusivity locally. Using a line laser oriented parallel to the gradient allows us to precisely measure the thermal diffusivity at small increments. The steps for the evaluation are set to 0.5 mm. The thermal diffusivity is calculated for each position on the gradient, represented by the white dotted line and the arrow (**Figure 3**a, b). From the amplitude and phase data of the gradient, the change in thermal conduction properties is directly observed. The white dash-dotted lines guide the eye to emphasize the change in thermal diffusivity along the carbon gradient. In both maps, the left side shows high thermal conductivity, whereas the right is significantly lower concomitant to the $FeCl_3$ impregnation. The results emphasize that no gradient in thermal diffusivity perpendicular to the dipping direction evolved. The obtained thermal diffusivity gradient is shown in Figure 3c. We observe a monotonic decrease in diffusivity along the gradient. The difference corresponds to a factor of *three* in a distance of around 15 mm. A comparison of the results with the diffusivity values from the homogeneous reference samples leads to a similar $FeCl_3$ concentration regime (<1 M) as deduced from the XRD and Raman analysis. This reveals a gradient in thermal conduction and diffusivity within the observed range. Similar to the thermal diffusivity measurements, the electrical sheet conductance gives a complementary picture of the gradient in the sample (Figure 3d). At the highest concentration point (0 mm), the conductance reaches a value of 0.68 S. Compared to the reference, that value fits in the range of <1 M as well. The conductance further decreases to 0.36 S, that is about 50% of the initial value.

Overall, the structural carbon gradient demonstrates transport properties that strongly depend on the $FeCl_3$ impregnation. As observed for the homogeneously modified reference samples,

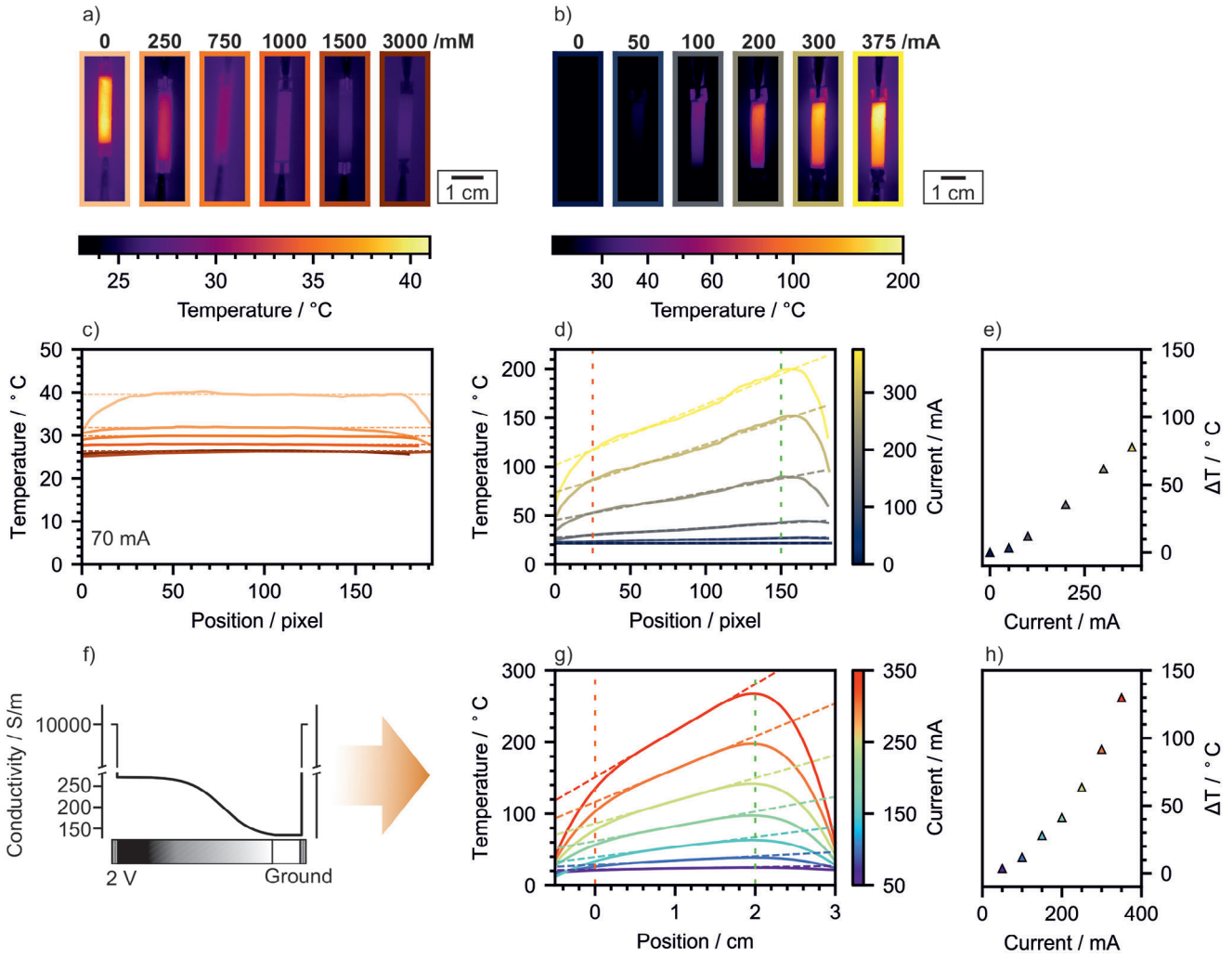

Figure 4. Joule heating experiments with reference and gradient samples. a) Thermograms of heated reference samples at 70 mA with various $FeCl_3$ concentration. b) Thermograms of the gradient samples with distinct currents from 0 to 375 mA. In (c), the mean temperatures from (a) are determined at the linear regime from 25 to 150 pixel. The temperature drops with higher concentrations, causing less sheet resistance from around 40 °C to about 26 °C. d) Temperature gradients extracted from (b). e) Temperature difference calculated from the minimum (red dashed line) and maximum (green dashed line) temperatures. The gradient regime is located between 25 to 150 pixel. At 375 mA, the difference reaches a maximum of nearly 80 °C. f) Model for the finite element method simulation. The model consists of the sample based on the data from the four-point probe and lock-in thermography measurements. Two metal heat sinks act as the contacting clips at both ends. g) Simulated temperature distribution for one gradient sample. They show a linear regime between0 to 20 mm. h) The temperature differences reach a maximum of 130 °C due to the absence of thermal losses in the simulation.

we see that the changes in the carbon microstructure affect heat and electron transport to a different extent. Whereas the sheet conductance only increases by a factor of about two between the boundaries of the gradient, the thermal diffusivity increases by a factor of about three. Even though the sheet conductance is considerable in this material, we assign the major contribution to thermal conduction to vibration-based transport along the carbon backbone. This is in line with other graphitic materials, where even in the case of much lower thermal transport properties, electronic heat transport played a minor role.[82]

Our carbon gradient structure can be expected to support strong and stable temperature gradients when applying an external current. The formation of a stable temperature gradient will be supported by the local combination of high sheet resistance and low thermal diffusivity. The first causes a high power input based on Joule heating, whereas the latter prevents the generated heat from being efficiently dissipated. An infrared (IR) camera was mounted above the samples to measure the emerging temperature profile. First, we heat the homogeneous reference samples with different iron concentrations. Due to the direct dependence of crystallinity on electrical and thermal conductivity, we expect an increase in temperature with poor crystallinity. We apply 70 mA to the reference samples. In the thermograms (**Figure** 4a), we observe uniformly distributed temperature profiles across the whole samples (Figure 4c). We see that a high crystallinity and high sheet conductance lead to a low average temperature, which is almost at room temperature. In total,

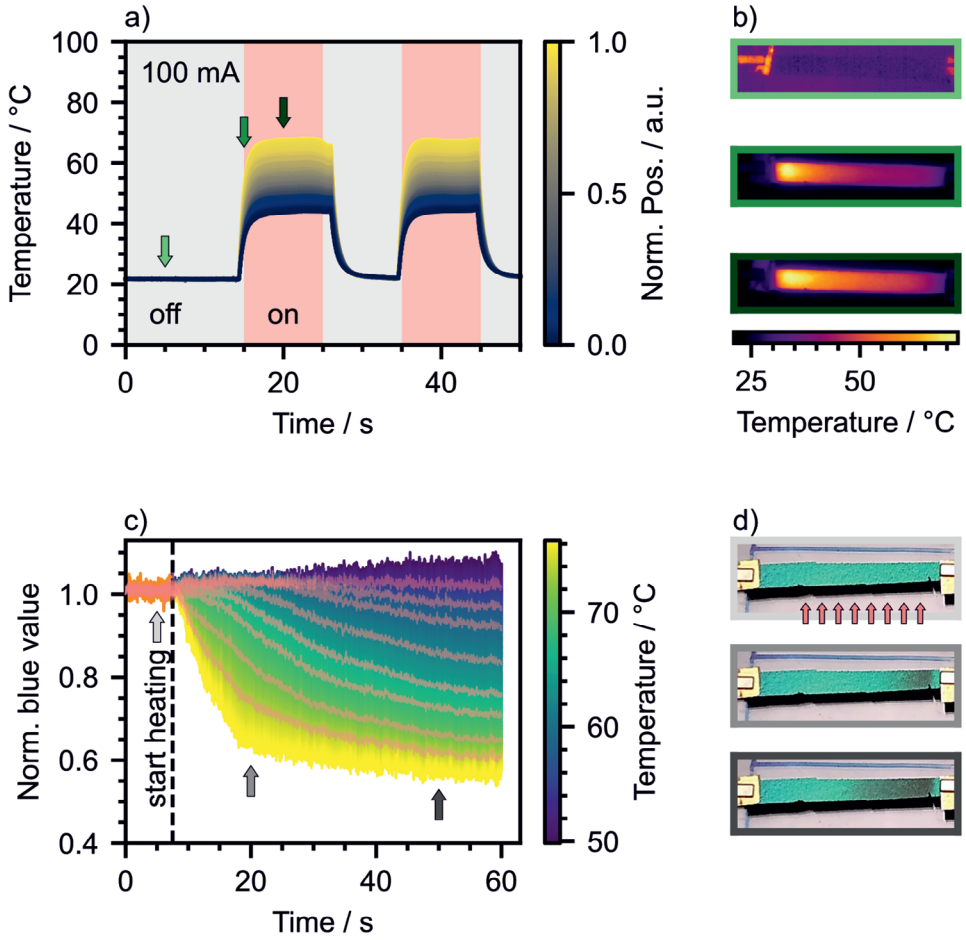

Figure 5. Controllable and stable temperature gradients. a) The sample shows fast switching properties at 100 mA. The temperature gradient ΔT = 30K builds up instantly and can be switched on and off repeatedly. b) Thermograms at different time steps during Joule heating. c) Evolution of the blue value of the photonic stopband of an immobilized colloidal crystal on a carbon gradient. Upon Joule heating, the temperature gradient builds up instantaneously. The heating was started at 7.5 s. A high temperature leads to fast film formation and loss of the blue color. d) Optical impression of the photonic stop band at distinct time steps during Joule heating (grey arrows). The red lines are guides to the eye and resemble distinct positions on the carbon gradient.

we achieve a temperature difference between high to low iron concentrations of 15 K. In contrast, we observe the immediate formation of a temperature gradient (Figure 4b) in the case of our gradient samples. When we apply rising currents from 0 to 375 mA, each temperature profile shows a linear increase between the boundaries and a systematic offset depending on the current (Figure 4d). The high-temperature end corresponds to low $FeCl_3$ concentration. Hence, the temperature delta between the minimum and maximum temperatures (dashed red and green lines) (Figure 4e) increases according to Joule's law. We observe a ΔT ≈80 K at 375 mA. With the help of finite element simulation (FEM), we verified these results. A model of the sample holder with one gradient sample was created (Figure 4f). We use the median electrical resistance data from the four-point probe measurement and thermal diffusivity data from lock-in thermography. Between both boundaries, the model applies a potential. The simulated temperature profile (Figure 4g, h) shows well comparable results. The temperature curves exhibit similar trends to those in the experiments. We observe a linear regime between 0 and 20 mm, too. In contrast to the experiments, the temperatures do not show thermal and electrical losses that exist in our experimental data. Hence, the simulation shows a higher maximum ΔT of circa 130 K.

We want to stress two distinct features of our gradient carbon material. First, we can translate the structural gradient into a pronounced temperature gradient that remains constant as long as a constant electrical current is applied. Second, we have a tool at hand to switch a temperature gradient on and off just by the electrical current and without the necessity to establish contact between a heat sink and source, respectively. To experimentally highlight both of these unique properties, we conducted two types of experiments. First, we measured the time evolution of the temperature gradient with the help of an IR camera. We observe fast switching properties (**Figure** 5a) within a few seconds. We see an instant development of a temperature gradient of ΔT = 30 K (Figure 5b). When switching off the current, the temperature directly relaxes to the ambient temperature. Further, we see that for every position on the gradient, the temperature is

reached equally fast. This process can be repeated several times. Second, we demonstrate that the temperature gradient can be transferred to another thin film material. Schöttle et al.[52] showed a system based on a mixture of low-T_g/high-T_g polymer nanoparticles of homogeneous size. In the form of a colloidal crystal, such particles show a structural coloration that can be used as time-temperature integrating sensors. These systems are based on their time-dependent film formation and concomitant loss of color. The rate of color loss strongly depends on the local temperature. Therefore, such colloidal films are ideal model sensors to map the temperature distribution along our carbon gradient samples. We use poly[(methyl methacrylate)-*random*-(butyl acrylate)] (PMMA-r-nBA) nanoparticles as a mixture of low-T_g and high-T_g (1: 1), 49 °C and 90 °C (Figure S14a,b, Supporting Information), respectively. They both have a diameter of 240 nm, resulting in a turquoise photonic stop band. The gradient sample is dip-coated with this particle mixture (Figure S14c,d, Supporting Information). In our setup (Figure S15, Supporting Information), we can measure the evolution of the photonic stop band and temperature simultaneously while applying a constant current (100 mA). The structural color is lost during the heating due to the film formation of the particles (Figure 5d). We see that with higher temperatures, the color loss is faster compared to areas of low temperatures. The evolution of the photonic stopband, thereby, represents the complete parameter space of time and temperature dependence along the carbon gradient. Owing to the direct connection between the lateral position, the blue value, and its temperature, we can assign a distinct temperature to each position (Figure 5c). Please note that the kinetics of the film formation are slower compared to the presence of the temperature gradient, which forms within a few seconds as shown in Figure 5a. We expect that the unique possibility of controlling temperature gradients with a high dynamic range will be relevant for various fields where temperature plays a pivotal role. For instance, measuring the Seebeck coefficient of thin film semiconductors requires well-controlled temperature gradients, for which clamped samples between a heat sink and source are still the most common measurement layout.[83] Further applications encompass battery research,[55,56] microfluidics[57,58] and continuous flow polymerase chain reaction.[59,60] Beyond that, such carbon gradient material can contribute to accelerate material science via efficient temperature screening experiments.[53,54]

3. Conclusion

We created a carbon material using laboratory-grade filter paper as the source. The paper is converted to a CM through catalytic carbonization while preserving its hierarchical structure. Using $FeCl_3$ as a catalyst in this process, we can vary the structural order significantly. Based on those insights, we introduced a straightforward way to control the structural order inside our CMs gradually. Using an infusion withdrawal setup consisting of two syringe pumps with different pumping rates, we gradually change the $FeCl_3$ solution along a strip of filter paper. After carbonization, the structural order changes gradually, as shown by Raman and XRD. Concomitantly, we also observe a monotonic increase in thermal and electrical conduction. Via Joule heating experiments, we achieved a large and steady temperature gradient of $\Delta T \approx 80$ °C across the gradient direction. These results were also confirmed by FEM simulation. Further, the produced material shows excellent and fast switching properties for the formation of thermal gradients, which can be applied to other materials, such as colloidal crystal thin films.

4. Experimental Section

Materials: Iron(III) chloride hexahydrate ($FeCl_3.6H_2O$) was obtained from Sigma–Aldrich and Honeywell Fluka. The 110 mm diameter filter paper (15A, 100% cellulose, 84 g m^{-2}, thickness 140 µm) was obtained from Carl Roth GmbH. The ferric chloride solutions were prepared using ultra pure water from a Merck Millipore Direct-Q 3UV. The contacting of the samples was performed using colloidal silver paint from Ted Pella Pelco.

Reference Preparation: Ferric chloride solutions with adjusted concentrations from 0.1 to 3 M were prepared in advance. In a standard petri dish, with a diameter of 70 mm, made from glass, 9 mL of the particular solution was added. A 3 mm diameter disk, cut out from the filter paper, was immersed in the solution for 3 h. Thereafter, the sample was retrieved, excess solution was removed, and dried at 80 °C for 25 min. Smaller diameter samples were stamped out. For the carbonization process, the samples were put between graphite plates. The oven was heated to 1500 °C under argon atmosphere with 100 K h^{-1}, followed by an 4 h isotherm and a cool down to room temperature. The iron residues were removed by immersing the carbonized samples in concentrated HCl for 24 h. The liquid was removed, and the samples were washed with concentrated HCl (37%) and twice with ethanol.

Gradient Preparation: The filter paper was cut into 70 mm long and 20 mm broad pieces. The sample was fixed in the lid of a water-filled snap lid glass. After 5 min, the water level was reduced to the upper mark of the sample. A 2 M $FeCl_3$ solution was pumped into the snap lid glass with a syringe pump at a rate of 1.16 mL min^{-1} (in total 11.6 mL). The solution in the snap lid glass was continuously stirred with a magnetic stirrer bar. Simultaneously, the overall solution level was lowered by a higher pumping rate of a second pump: 2.32 mL min^{-1} (in total 23.2 mL). This led to a continuous change of the immersion height while simultaneously increasing the $FeCl_3$ concentration. Due to the closed lid, water evaporation could be neglected at these time scales. Finally, the remaining solution was removed, and the sample was dried at 80 °C for 25 min. The carbonization process and the removal of the iron residue were performed as previously described.

Raman Spectroscopy: The measurements were conducted with a LabRAM HR from Horiba Jobin Yvon Raman Division, equipped with an Olympus BX41 microscope and a $\lambda = 635$nm, 11.5 mW HeNe laser. The resulting spectra were baseline-corrected with an algorithm from Zhang et al.[84] For each position on the gradient sample, a 3 mm disc was stamped out.

Confocal Raman Spectroscopy: A confocal WITec Alpha 300 RA+ Raman imaging system equipped with a UHTS 300 spectrometer and a back-illuminated Andor Newton 970 EMCCD camera together with the WITec Suite SIX 6.1 software package was employed for confocal Raman spectroscopy measurements. A laser intensity of 15 mW and an integration time of 0.5 s (grating: 600 g mm^{-1}) were employed. Single spectra were acquired with a 50 × long working distance objective (Zeiss LD EC Epiplan-Neofluar Dic 50 ×, numerical aperture NA = 0.55) using an excitation wavelength of $\lambda = 532$ nm, and 50 measurements were accumulated for a spectrum.

X-ray Scattering: Wide (WAXS) angle X-ray scattering experiments were performed on graphitic films on a lab-based Double Ganesha AIR system (SAXSLAB/Xenocs). This system was equipped with a copper rotating anode (MicroMax 007HF, Rigaku Corporation Japan, λ1.54 Å). WAXS data were recorded by a position-sensitive detector (PILATUS, 100K, Dectris). Additional measurements were performed at the beamline ID02 of the ESRF (European Synchrotron, Grenoble, France).[85] For ID02, the beam energy was set to 12.2 keV and simultaneous SAXS/WAXS measurements were performed using an Eiger2-4M for SAXS and a Rayonix LX170 for WAXS, spanning together a q range from 7×10^{-3} to 4.65 $Å^{-1}$. Data reduc-

tion and azimuthal integration were performed with software provided by ID02, including the software SAXSutilities2.[86] If needed, the 2D scattering patterns were converted to 1D profiles of $I(q)$ versus q, where q is given by $q = |\vec{q}| = \frac{4\pi}{\lambda} \sin \frac{\theta}{2}$ with θ being the scattering angle. Additionally, (powder) X-ray diffraction experiments (XRD) were carried out with a Bragg-Brentano geometry on a PANalytical Empyrean diffractometer (Malvern PANalytical BV, the Netherlands) equipped with a PIXcel^{1D}-Medipix3 detector in spinning mode using Cu K_α radiation ($\lambda = 1.5406$ Å). The instrument provided the PANalytical's Highscore Plus software for data analysis. For XRD measurements of the gradient, 3 mm discs were stamped out and ground down.

Atomic Absorption Spectroscopy: Iron-containing samples were treated with concentrated nitric acid for 24 h. 3 mL of the resulting solution were analyzed with an Analytic Jena contrAA300 high-resolution absorption spectrometer (Analytik Jena, Jena, Germany) equipped with a Xenon short-arc lamp (300 W, XBO 301, GLE Berlin, Germany) as a radiation source, a high-resolution double monochromator, e.g., a prism pre-monochromator and an echelle grating monochromator, and a charged-couple device array detector (CCD resolution about 2 pm pixel^{-1} in the far UV range). Measurements were performed at 248.3 nm using an oxidizing air/acetylene flame. Iron species content was given as mean value in µg L^{-1} (averaged values of three experiments measured in quintuplicates).

Lock-in Thermography: Lock-in thermography (LIT) was conducted in rear-face configuration. The sample was placed in an aluminum vacuum chamber ($p < 1 \times 10^{-2}$mbar) on top of a three-axis translation stage and a tip-tilt rotation stage. A line laser (13LR12-M125 + 55CM-520-56-O08-T15-PS-7, Schäfter+Kirchhoff GmbH) with a $\lambda = 520$ nm at 55 mW enters the chamber through an optical transparent glass window (N-BK7). The detection was performed by an IR camera (Image IR 9400, InfrTec GmbH) through a sapphire window with synchronization by Infra Tec's IR-BIS activeonline software. The camera's frame rate was set to 100 frames per second. Measurements were taken with a 1 × lens with a pixel resolution of 10µm. The equilibrium time per measurement was 60 s or 50 periods, whichever was longer. The measurement time was set to 60 s. For frequency-dependent measurements, the excitation frequency was logarithmically varied from 0.1 to 25 Hz.

Joule Heating: The samples were contacted with conductive silver paint and copper foil. The samples were connected via clamps to an Aim TTi PLH250 DC power supply. The sample was illuminated with a full-spectrum lamp (Walimax pro LED Niova 600 Plus Daylight) with a light diffuser at an angle of 10° and 30 cm distance. Color videos (30 fps, FHD, ISO 800, 1/19164 s exposure time) were recorded with a smartphone (Fairphone 3+) and saved in the mp4 format. The IR data was collected with an InfraTec VarioCAM HD research IR camera (7.5 to 14 µm) with 30 fps. The video data was separated into single frames. For every frame, color and IR data were extracted along a line on the gradient axis.

Four-Point Probe: Measurements were conducted on a self-built setup. Four spring probe pin electrodes (NP58-N, MISUMI Europa GmbH) with 0.42 mm spherical, rhodium coated tips were equally distributed with 1 mm distance on a 3D printed mount fixed to a force pressure sensor. The electrodes were connected to a Keithley 2400 multimeter. The measurement was conducted under constant current. The gradient samples were measured with a step size of 2 mm.

Scanning Electron Microscopy: Images were taken with a Zeiss Leo 1530 or the Zeiss Ultra plus (both Carl Zeiss AG, Germany) at 3 to 10 kV with secondary electron and in-lens detection without platinum sputtering.

Laser Scanning Confocal Microscopy: Both 2D color images and 3D reconstructed images were taken with a laser scanning confocal microscope (Olympus, OLS5000) with a white light source and a 405 nm laser. Images were obtained mostly by 20 × lens with NA. 0.45. Overviews of the gradient were obtained by the software's stitching mode.

Density Measurements: Density measurements were performed on an Ultrapyc 1200e (Quantachrome Instruments) with Helium 5.0. The average density and standard deviation were determined using 25 individual measurements.

Finite Element Simulation: The Joule heating performance of the samples was calculated with Finite element simulations (FEM), combining the heat transfer interface of COMSOL Multiphysics with the electric current module. A 1D model of the sample's electrical properties, namely the electrical resistance, was used to calculate the amount of heat produced by currents from 0 to 350 mA. For a correct reproduction of the Joule heating measurement setup, two heat sinks at the ends of the samples were added, representing the metal clips used for the fixation and contacting of the samples. The electrical resistance data was taken from the median of the four-point probe measurements along the sample and implemented as an analytical function. The density was approximated to 110 kg m^{-3} by weight and thickness. The mean specific heat capacity was determined by dynamic scanning calorimetry (DSC) measurements (ASTM E1269) to be 820 J kg^{-1} K^{-1}. The sample's relative permittivity ε_r was set to 12, which was in the range of graphite.

Supporting Information

Supporting Information is available from the Wiley Online Library or from the author.

Acknowledgements

A.B. and M.S. thank the Elite Network of Bavaria (ENB). F.L. acknowledged support from the Bavarian Center for Battery Technology (BayBatt). The authors thank Prof. Jürgen Senker for fruitful discussions on the XRD evaluation. Help from Keylab Electron Microscopy and Maximilian Theis in conducting SEM measurements is appreciated. Special thanks to Stefan Rettinger for his continuous support and lab service. The authors thank Prof. Dirk Schüler for providing access to AAS measurements. Additionally, the authors are grateful for the measurements performed at the beamline ID02 at ESRF in Grenoble, France. This work had been supported by Collaborative Research Center 1585, Project C05 of the German Research Foundation (Grant number 492723217).

Open access funding enabled and organized by Projekt DEAL.

Conflict of Interest

The authors declare no conflict of interest.

Data Availability Statement

The data that support the findings of this study are available from the corresponding author upon reasonable request.

Keywords

catalytic graphitization, carbon microstructure, electron transport, heat transport, infusion withdrawal coating

Received: January 13, 2024
Revised: July 12, 2024
Published online: August 24, 2024

[1] A. Pragya, T. K. Ghosh, *Adv. Mater.* **2023**, *35*, 49.
[2] J. Liu, J. Zhou, M. Wang, C. Niu, T. Qian, C. Yan, *J. Mater. Chem.A* **2019**, *7*, 24477.
[3] Z. Zhang, S. Ren, *ACS Appl. Polym. Mater.* **2019**, *1*, 2197.
[4] Q. Liu, W. Gong, S. Li, C. Zhao, D. Xu, Y. Liu, Z. Yang, X. Bai, A. Ying, *J. Power Sources* **2021**, *515*, 230621.

[5] M. Chen, K. Hagedorn, H. Cölfen, S. Polarz, *Adv. Mater.* **2016**, *29*, 2.
[6] J. Bahner, N. Hug, S. Polarz, *C* **2021**, *7*, 22.
[7] J. Bahner, N. Klinkenberg, M. Frisch, L. Brauchle, S. Polarz, *Adv. Funct. Mater.* **2019**, *29*, 44.
[8] M. Evers, K. Hauser, W. G. Hinze, N. Klinkenberg, Y. Krysiak, D. Mombers, S. Polarz, *J. Mater. Chem.A* **2024**, *12*, 11332.
[9] M. Giese, L. K. Blusch, M. K. Khan, M. J. MacLachlan, *Angew. Chem. Int. Ed.* **2015**, *54*, 2888.
[10] R. J. Moon, A. Martini, J. Nairn, J. Simonsen, J. Youngblood, *Chem. Soc. Rev.* **2011**, *40*, 3941.
[11] T. Li, C. Chen, A. H. Brozena, J. Y. Zhu, L. Xu, C. Driemeier, J. Dai, O. J. Rojas, A. Isogai, L. Wågberg, L. Hu, *Nature* **2021**, *590*, 47.
[12] D. Klemm, B. Heublein, H.-P. Fink, A. Bohn, *Angew. Chem.* **2005**, *117*, 3422.
[13] D. Tobjörk, R. Österbacka, *Adv. Mater.* **2011**, *23*, 1935.
[14] M. Berggren, D. Nilsson, N. D. Robinson, *Nat. Mater.* **2007**, *6*, 3.
[15] A. C. Siegel, S. T. Phillips, M. D. Dickey, N. Lu, Z. Suo, G. M. Whitesides, *Adv. Funct. Mater.* **2010**, *20*, 28.
[16] D.-H. Kim, Y.-S. Kim, J. Wu, Z. Liu, J. Song, H.-S. Kim, Y. Y. Huang, K.-C. Hwang, J. A. Rogers, *Adv. Mater.* **2009**, *21*, 3703.
[17] A. Asadpoordarvish, A. Sandström, C. Larsen, R. Bollström, M. Toivakka, R. Österbacka, L. Edman, *Adv. Funct. Mater.* **2015**, *25*, 3238.
[18] J.-L. Schäfer, T. Meckel, S. Poppinga, M. Biesalski, *Biomimetics* **2023**, *8*, 43.
[19] X. Ming, A. Wei, Y. Liu, L. Peng, P. Li, J. Wang, S. Liu, W. Fang, Z. Wang, H. Peng, J. Lin, H. Huang, Z. Han, S. Luo, M. Cao, B. Wang, Z. Liu, F. Guo, Z. Xu, C. Gao, *Adv. Mater.* **2022**, *34*, 2201867.
[20] M. Wissler, *J. Power Sources* **2006**, *156*, 142.
[21] Z.-Y. Wu, S.-L. Xu, Q.-Q. Yan, Z.-Q. Chen, Y.-W. Ding, C. Li, H.-W. Liang, S.-H. Yu, *Sci. Adv.* **2018**, *4*, eaat0788.
[22] A. D. Avery, B. H. Zhou, J. Lee, E.-S. Lee, E. M. Miller, R. Ihly, D. Wesenberg, K. S. Mistry, S. L. Guillot, B. L. Zink, Y.-H. Kim, J. L. Blackburn, A. J. Ferguson, *Nat. Energy* **2016**, *1*, 1.
[23] J. L. Blackburn, A. J. Ferguson, C. Cho, J. C. Grunlan, *Adv. Mater.* **2018**, *30*, 1704386.
[24] C. Wang, K. Xia, H. Wang, X. Liang, Z. Yin, Y. Zhang, *Adv. Mater.* **2019**, *31*, 1801072.
[25] Y. Cohen, A. Ya'akobovitz, *Nanotechnology* **2021**, *33*, 345703.
[26] C. Geng, Y.-x. Chen, L.-l. Shi, Z.-f. Sun, L. Zhang, A.-y. Xiao, J.-m. Jiang, Q.-c. Zhuang, Z.-c. Ju, *New Carbon Mater.* **2022**, *37*, 461.
[27] T.-y. Wang, H.-b. Huang, H.-l. Li, Y.-k. Sun, Y.-h. Xue, S.-n. Xiao, J.-h. Yang, *New Carbon Mater.* **2021**, *36*, 683.
[28] H. Wang, Y. Shao, S. Mei, Y. Lu, M. Zhang, J. K. Sun, K. Matyjaszewski, M. Antonietti, J. Yuan, *Chem. Rev.* **2020**, *120*, 9363.
[29] Y. J. O. Asencios, V. S. Lourenço, W. A. Carvalho, *Catal. Today* **2022**, *388–389*, 247.
[30] Z. Wang, M. Zhang, W. Ma, J. Zhu, W. Song, *Small* **2021**, *17*, 2100219.
[31] M. Liu, Y. Wang, F. Wu, Y. Bai, Y. Li, Y. Gong, X. Feng, Y. Li, X. Wang, C. Wu, *Adv. Funct. Mater.* **2022**, *32*, 2203117.
[32] H. Ren, M. Tang, B. Guan, K. Wang, J. Yang, F. Wang, M. Wang, J. Shan, Z. Chen, D. Wei, H. Peng, Z. Liu, *Adv. Mater.* **2017**, *29*, 1702590.
[33] H. Ghasemi, G. Ni, A. M. Marconnet, J. Loomis, S. Yerci, N. Miljkovic, G. Chen, *Nat. Commun.* **2014**, *5*, 1.
[34] S. P. Surwade, S. N. Smirnov, I. V. Vlassiouk, R. R. Unocic, G. M. Veith, S. Dai, S. M. Mahurin, *Nat. Nanotechnol.* **2015**, *10*, 459.
[35] M.-M. Titirici, M. Antonietti, *Chem. Soc. Rev.* **2010**, *39*, 103.
[36] E. Berl, A. Schmidt, *Justus Liebigs Ann. Chem.* **1932**, *493*, 97.
[37] M. M. Titirici, A. Thomas, S.-H. Yu, J.-O. Müller, M. Antonietti, *Chem. Mater.* **2007**, *19*, 4205.
[38] D. Zhai, H. Du, B. Li, Y. Zhu, F. Kang, *Carbon* **2011**, *49*, 725.
[39] A. Gomez-Martin, Z. Schnepp, J. Ramirez-Rico, *Chem. Mater.* **2021**, *33*, 3087.
[40] A. Ōya, S. Ōtani, *Carbon* **1979**, *17*, 131.
[41] A. Ōya, H. Marsh, *J. Mater. Sci.* **1982**, *17*, 309.
[42] M. Sevilla, A. B. Fuertes, *Carbon* **2006**, *44*, 468.
[43] F. J. Maldonado-Hódar, C. Moreno-Castilla, J. Rivera-Utrilla, Y. Hanzawa, Y. Yamada, *Langmuir* **2000**, *16*, 4367.
[44] C. J. Thambiliyagodage, S. Ulrich, P. T. Araujo, M. G. Bakker, *Carbon* **2018**, *134*, 452.
[45] A. Gutiérrez-Pardo, J. Ramírez-Rico, R. Cabezas-Rodríguez, J. Martínez-Fernández, *J. Power Sources* **2015**, *278*, 18.
[46] M.-M. Titirici, R. J. White, C. Falco, M. Sevilla, *Energy Environ. Sci.* **2012**, *5*, 6796.
[47] Y. Huang, Y. Chen, X. Fan, N. Luo, S. Zhou, S. C. Chen, N. Zhao, C. P. Wong, *Small* **2018**, *14*, 1801520.
[48] J. Cai, H. Niu, Z. Li, Y. Du, P. Cizek, Z. Xie, H. Xiong, T. Lin, *ACS Appl. Mater. Interfaces* **2015**, *7*, 14946.
[49] H. Zhuo, Y. Hu, X. Tong, Z. Chen, L. Zhong, H. Lai, L. Liu, S. Jing, Q. Liu, C. Liu, X. Peng, R. Sun, *Adv. Mater.* **2018**, *30*, 1706705.
[50] Z. Ding, F. Li, J. Wen, X. Wang, R. Sun, *Green Chem.* **2018**, *20*, 1383.
[51] S. Glatzel, Z. Schnepp, C. Giordano, *Angew. Chem. Int. Ed.* **2013**, *52*, 2355.
[52] M. Schoettle, T. Tran, T. Feller, M. Retsch, *Adv. Mater.* **2021**, *33*, 2101948.
[53] D. O'Nolan, G. Huang, G. E. Kamm, A. Grenier, C.-H. Liu, P. K. Todd, A. Wustrow, G. Thinh Tran, D. Montiel, J. R. Neilson, S. J. L. Billinge, P. J. Chupas, K. S. Thornton, K. W. Chapman, *J. Appl. Crystallogr.* **2020**, *53*, 662.
[54] J. S. O. Evans, I. Radosavljević Evans, *Chem. Soc. Rev.* **2004**, *33*, 539.
[55] R. Carter, T. A. Kingston, R. W. Atkinson, M. Parmananda, M. Dubarry, C. Fear, P. P. Mukherjee, C. T. Love, *Cell Rep. Phys. Sci.* **2021**, *2*, 100351.
[56] M. Naylor Marlow, J. Chen, B. Wu, *Comm. Eng.* **2024**, *3*, 1.
[57] A. A. Dos-Reis-Delgado, A. Carmona-Dominguez, G. Sosa-Avalos, I. H. Jimenez-Saaib, K. E. Villegas-Cantu, R. C. Gallo-Villanueva, V. H. Perez-Gonzalez, *Electrophoresis* **2022**, *44*, 268.
[58] S. M. Shameli, T. Glawdel, Z. Liu, C. L. Ren, *Anal. Chem.* **2012**, *84*, 2968.
[59] Z. E. Jeroish, K. S. Bhuvaneshwari, F. Samsuri, V. Narayanamurthy, *Biomed. Microdevices* **2021**, *24*, 1.
[60] N. Crews, C. Wittwer, B. Gale, *Biomed. Microdevices* **2007**, *10*, 187.
[61] M. N. Costa, B. Veigas, J. M. Jacob, D. S. Santos, J. Gomes, P. V. Baptista, R. Martins, J. Inácio, E. Fortunato, *Nanotechnology* **2014**, *25*, 094006.
[62] S. H. Park, S. M. Jo, D. Y. Kim, W. S. Lee, B. C. Kim, *Synth. Met.* **2005**, *150*, 265.
[63] Z. Q. Li, C. J. Lu, Z. P. Xia, Y. Zhou, Z. Luo, *Carbon* **2007**, *45*, 1686.
[64] F. Tuinstra, J. L. Koenig, *J. Chem. Phys.* **1970**, *53*, 1126.
[65] L. G. Cançado, K. Takai, T. Enoki, M. Endo, Y. A. Kim, H. Mizusaki, A. Jorio, L. N. Coelho, R. Magalhães-Paniago, M. A. Pimenta, *Appl. Phys. Lett.* **2006**, *88*, 163106.
[66] A. Philipp, N. W. Pech-May, B. A. F. Kopera, A. M. Lechner, S. Rosenfeldt, M. Retsch, *Anal. Chem.* **2019**, *91*, 8476.
[67] A. Wolf, P. Pohl, R. Brendel, *J. Appl. Phys.* **2004**, *96*, 6306.
[68] J. Lienhard, *Heat Transfer Textbook Fifth Edition*, Dover Publications, New York **2019**.
[69] B. N. Enweani, J. W. Davis, A. A. Haasz, *J. Nucl. Mater.* **1995**, *224*, 245.
[70] M. R. Null, W. W. Lozier, A. W. Moore, *Carbon* **1973**, *11*, 81.
[71] Y. Rhim, D. Zhang, M. Rooney, D. C. Nagle, D. H. Fairbrother, C. Herman, D. G. Drewry, *Carbon* **2010**, *48*, 31.
[72] S. Bard, T. Tran, F. Schönl, S. Rosenfeldt, M. Demleitner, H. Ruckdäschel, M. Retsch, V. Altstädt, *Carbon Lett.* **2023**, *34*, 361.
[73] M. Minus, S. Kumar, *JOM* **2005**, *57*, 52.
[74] M. Han, D. Mao, T. Liang, E. Gao, X. Bai, X. Zeng, R. Sun, J. Xu, *Carbon* **2022**, *195*, 319.
[75] R. Matsumoto, Y. Okabe, *Synth. Met.* **2016**, *212*, 62.
[76] D. Van Tuan, J. Kotakoski, T. Louvet, F. Ortmann, J. C. Meyer, S. Roche, *Nano Lett.* **2013**, *13*, 1730.

[77] G. Fugallo, A. Cepellotti, L. Paulatto, M. Lazzeri, N. Marzari, F. Mauri, *Nano Lett.* **2014**, *14*, 6109.
[78] T. Ma, Z. Liu, J. Wen, Y. Gao, X. Ren, H. Chen, C. Jin, X.-L. Ma, N. Xu, H.-M. Cheng, W. Ren, *Nat. Commun.* **2017**, *8*, 1.
[79] J. Gao, H. Zobeiri, H. Lin, D. Xie, Y. Yue, X. Wang, *Carbon* **2021**, *178*, 92.
[80] M. Schöttle, M. Theis, T. Lauster, S. Hauschild, M. Retsch, *Adv. Opt. Mater.* **2023**, *11*, 16.
[81] F. Ye, C. Cui, A. Kirkeminde, D. Dong, M. M. Collinson, D. A. Higgins, *Chem. Mater.* **2010**, *22*, 2970.
[82] X. Liao, J. Denk, T. Tran, N. Miyajima, L. Benker, S. Rosenfeldt, S. Schafföner, M. Retsch, A. Greiner, G. Motz, S. Agarwal, *Sci. Adv.* **2023**, *9*, 13.
[83] D. Beretta, P. Bruno, G. Lanzani, M. Caironi, *Rev. Sci. Instrum.* **2015**, *86*, 7.
[84] Z.-M. Zhang, S. Chen, Y.-Z. Liang, *Analyst* **2010**, *135*, 1138.
[85] T. Narayanan, M. Sztucki, T. Zinn, J. Kieffer, A. Homms-Puron, J. Gorini, P. Van Vaerenbergh, P. Boesecke, *J. Appl. Crystallogr.* **2022**, *55*, 98.
[86] M. Sztucki, SAXSutilities2: a graphical user interface for processing and analysis of Small-Angle X-ray Scattering data (1.024), Zenodo, **2021**, https://doi.org/10.5281/zenodo.5825707.